Progress in Additive Manufacturing (2025) 10:6797–6804
https://doi.org/10.1007/s40964-025-01007-6

FULL RESEARCH ARTICLE

Additive manufacturing of $Ni_{62}Nb_{38}$ metallic glass via laser powder bed fusion

Maximilian Frey[1] · Jan Wegner[2] · Lucas Matthias Ruschel[1] · Erika Soares Barreto[3,4] · Sascha Sebastian Riegler[1] · Bastian Adam[1] · Nils Ellendt[3,4] · Stefan Kleszczynski[2,5] · Ralf Busch[1]

Received: 8 March 2024 / Accepted: 30 January 2025 / Published online: 26 February 2025

Abstract
The binary $Ni_{62}Nb_{38}$ bulk metallic glass exhibits attractive mechanical properties like a yield strength of more than 3 GPa and a hardness of more than 900 Vickers. Due to its limited glass forming ability in casting processes, industrial applications of this impressive material are still pending. Additive manufacturing via laser powder bed fusion (PBF-LB/M) can allow to overcome these limitations. Therefore, we present the first PBF-LB/M parameter study on $Ni_{62}Nb_{38}$. We are able to achieve high densification and almost fully amorphous samples, thereby demonstrating the general applicability of PBF-LB/M to process binary amorphous Ni–Nb alloys. Furthermore, two challenges can be identified, which have to be addressed before additively formed $Ni_{62}Nb_{38}$ can be considered for commercial use. Future parameter fine-tuning must lead to fully vitrified samples, and one must also find a way to avoid crack formation during processing, which was found to be one of the main issues in the present study.

Keywords Metallic glass · Amorphous metal · Additive manufacturing · Selective laser melting · Laser powder bed fusion

1 Introduction

Bulk metallic glasses (BMGs) feature favorable material properties that result from their amorphous structure. High strength, hardness, and, for metals, exceptionally large elastic limits of about 2% constitute a disruptive potential for structural applications [1]. To obtain a metallic glass, the high-temperature melt must be quenched fast enough to ensure complete vitrification without crystallization. The slowest cooling rate that avoids crystallization is termed the critical cooling rate R_C, which is a direct measure of the alloys glass forming ability (GFA). In terms of classical casting routes, geometry-dependent heat dissipation implies that the R_C results in a critical casting thickness, D_C, the largest diameter, to which a fully amorphous rod can be cast. For most BMGs, D_C is of the order of several millimeters [1], which limits the industrial applicability of BMGs. Yet, advances in process engineering have opened a new range of possibilities. Laser powder bed fusion of metals (PBF-LB/M) is a layer-wise additive manufacturing technique that uses rapid laser scanning to locally melt powder material and compact it during solidification. The process features small melt pools with diameters of about 100 µm and is associated with cooling rates of about 10^6 K/s [2, 3]. Hence, cooling and vitrification are decoupled from the size of the final part, allowing to overcome the geometrical limitations of cast BMGs as demonstrated by various studies presenting large and complex shapes [4–8]. However, previous investigations on PBF-LB/M processing of BMGs predominantly targeted the fabrication of established glass formers such as Zr- [5, 9–14], Ti- [15], CuTi- [16], or Fe-based [4, 8] BMGs. For example, AMZ4 [17] ($Zr_{59.3}Cu_{28.8}Al_{10.4}Nb_{1.5}$, also termed Zr01) and Vit101 ($Cu_{47}Ti_{34}Zr_{11}Ni_8$) can reproducibly reach their yield strength before brittle fracture occurs, but BMGs are still mediocre with strength values of, respectively, 2.1

✉ Maximilian Frey
maximilian.frey@uni-saarland.de

1 Chair of Metallic Materials, Saarland University, Saarbrücken, Germany

2 Chair of Manufacturing Technology, University of Duisburg-Essen, Duisburg, Germany

3 Leibniz Institute for Materials Engineering—IWT, Bremen, Germany

4 Faculty of Production Engineering, University of Bremen, Bremen, Germany

5 Center for Nanointegration Duisburg-Essen (CENIDE), Duisburg, Germany

[11, 18] and 2.5 GPa [16] in bending. At this point, Ni–Nb alloys [19] appear as promising candidates to exceed these numbers considerably. The simple binary $Ni_{62}Nb_{38}$ system exhibits a D_C of 2 mm [20] and can reach a yield strength between 3 and 3.5 GPa [21], thereby outperforming Zr- and CuTi-based systems by about 1 GPa. Combined with the exceptional elastic limit typical for BMGs and hardness values of more than 900 Vickers [21–23], Ni–Nb-based metallic glasses outrival most metallic materials, including high-performance steels [24]. The comparably low GFA of the Ni–Nb system prohibited vitrification in an earlier additive manufacturing approach using laser based direct energy deposition (LB-DED), a method that features cooling rates in the order of 10^2 to 10^4 K/s [25]. In the present work, we provide the first attempt to use laser powder bed fusion (PBF-LB/M) to process the binary $Ni_{62}Nb_{38}$ alloy. Thereby, we try to find processing parameters that result in highly dense, crack-free, and fully amorphous samples, since only this combination will allow for the most mechanically robust and performant parts [11, 16, 26]. Due to the small amount of powder feedstock that is available from the atomization process [27], we are limited to a first preliminary parameter evaluation. Nevertheless, we will show that we are able to reach almost fully amorphous samples, demonstrating the applicability of PBF-LB/M processing of amorphous $Ni_{62}Nb_{38}$ alloys. Furthermore, we can identify main issues that have to be addressed in the future before the system can be introduced to industrial applications. In particular, crack formation has to be diminished to allow for robust parts.

2 Experimental

The atomization and evaluation of the powder feedstock that is used in the present study are described in detail in a previous study by Barreto et al. [27]. To quickly recapitulate, elemental Ni (99.95 wt%) and Nb (99.9 wt%) were weighed to match the desired composition of $Ni_{62}Nb_{38}$ (at%) and were further pre-alloyed by arc-melting under Ti-gettered Ar atmosphere. To ensure chemical homogeneity, the ingots were flipped and remelted at least five times. The ingots were then gas-atomized into about 500 g of powder feedstock using graphite crucibles. The powder was sieved and a size distribution of 20–63 µm was chosen for further use. PBF-LB/M processing was conducted on an SLM 280 HL Twin laser system. The operating 700 W lasers have a focal diameter of about 70 µm. Argon was used as the shielding gas, resulting in a residual oxygen concentration of 0.05 vol.% in the chamber. No heating of the build plate was applied. The process parameters were evaluated by varying the scan speed, v, and the laser power, P, to form cuboid samples ($4 \times 6.5 \times \sim 1$ mm). Layer height, d, and hatch distance, h, were held constant at $d = 40$ µm and $h = 100$ µm. The resulting volume energy densities, E_V, can be calculated as:

$$E_V = \frac{P}{vdh}$$

Cuboids were created with E_V values ranging between 13.3 and 49.3 J/mm^3, as listed in Table 1 (one 100 W parameter combination was excluded from the list and from further analysis due to extreme brittleness and sample loss). A detailed explanation of the principles of the PBF-LB/M process can be found in [26].

Each parameter setting was investigated for two different scanning strategies. For the first one, parallel scanning vectors to the sample edges were applied. Hence, the laser tracks of subsequent layers share the same orientation. The second sample set was processed using a rotating scanning strategy, which shifts the vector orientation by 67° in reference to the previous layer. Figure 1 shows the manufactured samples on the build plate and further explains both scanning strategies.

The processed samples were cut in half, perpendicular to their building direction. One half was embedded, sanded, and polished for optical microscopy and optical relative density determination, which was performed using an Olympus BX51M and the image analysis software Stream essentials version 1.9.4. Some of these samples were further characterized by micro-hardness testing (HV1) using a Zwick Z3212 (Zwick Roell) hardness tester. Five indents per sample allow for statistics. The second half was investigated with X-ray diffraction (XRD) and differential thermal analysis (DTA). For the XRD analysis, a Bruker D8-A25-Advance diffractometer was used applying Cu-K_α-radiation with a wavelength of 1.5406 Å between the angles (2θ) of 20° to 80°. DTA temperature scans on selected cuboids were performed in Y_2O_3 coated carbon crucibles using a Netzsch STA 449 F3 Jupiter device applying heating scans with a rate of 0.33 K/s from 293 to 1050 K under high-purity argon flow. Scanning electron microscopy (SEM) was performed on polished sample surfaces using a Zeiss Sigma VP device. Thereby, energy-dispersive X-ray spectroscopy (EDX) was

Table 1 Process parameters used for PBF-LB/M

P (W)	v (mm/s)	E_V (J/mm^3)
100	530	47.2
100	940	26.6
150	760	49.3
150	1190	31.5
150	2110	17.8
200	1350	37.0
200	2100	23.8
200	3750	13.3

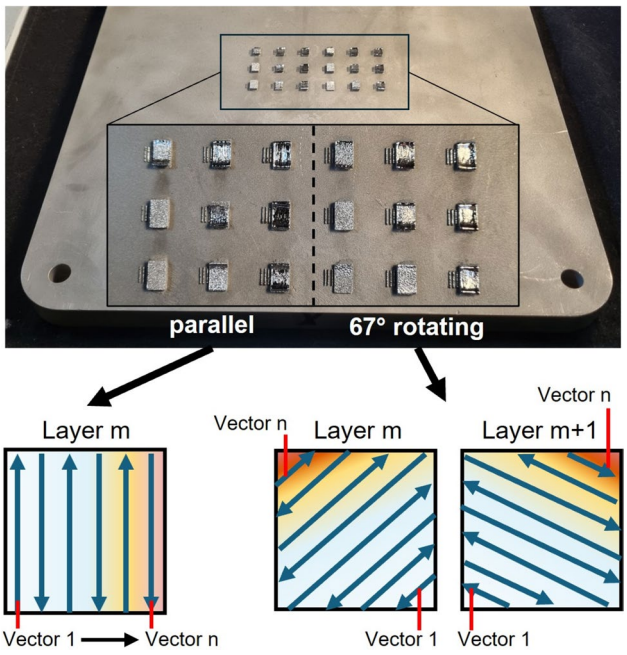

Fig. 1 A photo of the manufactured samples. Both scanning strategies are explained below. While the parallel vectors strategy uses the same scanning pattern for every layer, the rotating vectors strategy changes the vector orientation between consecutive layers through a 67° rotation

performed in area scanning mode to allow for elemental mapping.

3 Results and discussion

3.1 Density and hardness evaluation

Figure 2a displays the cross-sectional optical micrographs of three parallel vector cuboids, which represent the whole spectrum of used volume energy densities (49.3, 31.5, and 17.8 J/mm^3, respectively). As expected, the overall sample density rises with increasing E_V (the used energy range was not high enough to observe a density decrease due to keyholing). The higher energy input allows to eliminate lack of fusion, resulting in decreased porosity due to improved compaction of the molten powder material, as reported in a number of earlier studies [28–31]. Yet, with rising E_V and increased density, a tendency to form cracks is also observed in the samples, see e.g. the 31.5 J/mm^3 sample in Fig. 2a. This can be mainly attributed to the temperature gradients that arise during PBF-LB/M processing. These predominantly create in-plane residual stresses [32, 33], and hence, most of the cracks are oriented horizontally. Figure 2b shows the optically determined relative density (blue circles) and HV1 hardness (red squares) of the parallel vector cuboids as a function of the applied E_V. Both parameters increase with increasing E_V, reflecting the improved material compaction, which leads to relative densities of up to 99.9%. By

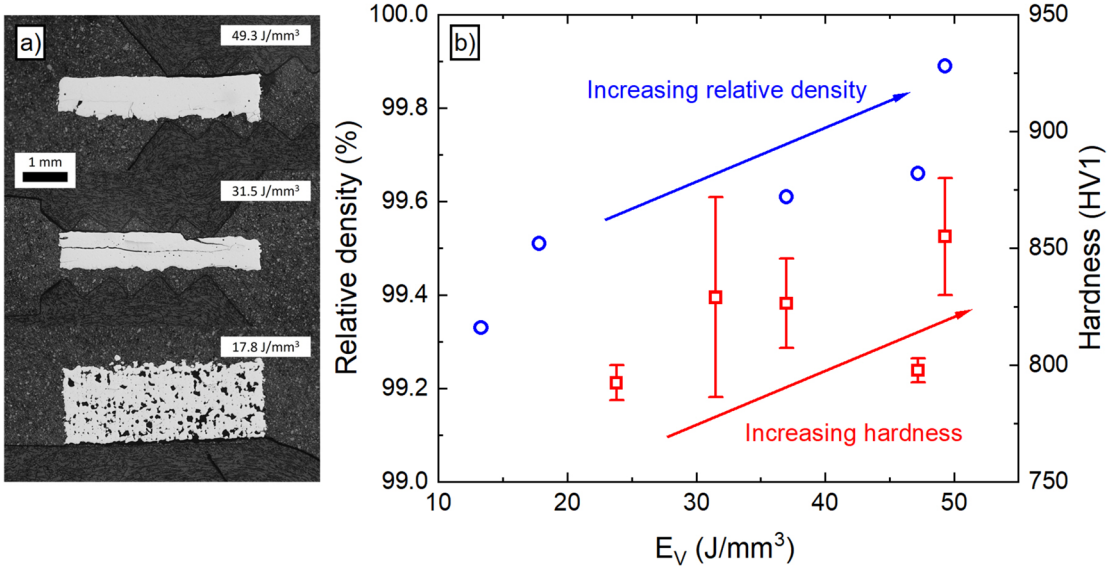

Fig. 2 **a** Optical micrographs of cross-sections of three representative parallel vector cuboids with different volume energy densities. Porosity decreases with increasing E_V, yet crack formation is observed in the more compacted samples. **b** A comparison of relative density (blue circles) and HV1 hardness (red squares) of the parallel vector cuboids. Both quantities rise with increasing E_V, allowing for densities of up to 99.9% and hardness values of almost 900 HV1. (Due to sample loss through brittle fracture, the shown data sets are incomplete)

approaching levels of 900 HV1, the samples feature the typical extreme hardness of Ni-Nb-based metallic glass formers [21–23].

3.2 *Amorphicity screening* via *X-ray diffraction*

A first screening in terms of the amorphous state of the samples is given in Fig. 3, where the diffractograms of cuboids formed with parallel and rotating vectors are compared. In the case of parallel vectors, broad diffraction halos suggest mostly amorphous samples, except for the sample with the highest E_V of 49.3 J/mm^3, which indicates partial crystallization in the form of arising Bragg reflections. Here, the high energy input appears to promote crystal formation, as previously reported by various studies [5, 10, 11]. In contrast, the cuboids formed with rotating vectors seem to be more prone to crystallization. On the one hand, the sample produced with a high E_V value of 49.3 J/mm^3 features more distinct Bragg reflections as its parallel vector counterpart, suggesting a larger crystalline fraction. On the other hand, the low-energy rotating vector samples (13.3 and 17.8 J/mm^3) also show distinct reflections. We interpret this as the result of two effects. First, the high degree of porosity of these low-E_V cuboids (see Fig. 2) might decrease the overall heat dissipation capability of the sample, resulting in local heat accumulations that promote crystallization. Similar observations have been reported in the case of CuTi-based samples formed by PBF-LB/M [16]. Yet, the low-E_V parallel vector cuboids in Fig. 3a do not show Bragg reflections, and therefore, we assume, secondly, that the rotating vector strategy induces additional overheating at the edges of the cubic samples due to shorter vector lengths, which would then lead to the higher degree of crystallinity in those samples. In Fig. 3c, we take a closer look at the samples that show the most prominent Bragg reflections, namely the rotating vector cuboids formed with 49.3 J/mm^3, 17.8 mm^3, and 13.3 mm^3. The peaks can be mostly attributed to the crystalline equilibrium phases Ni_6Nb_7 and Ni_3Nb that appear in the binary Ni–Nb phase diagram [34]. Furthermore, Ni_2O_3 can be identified, which is likely a consequence of the relatively high oxygen content of the used powder feedstock (863 ± 9 wt-ppm as reported in [27]).

3.3 Identification of crystalline precipitations through electron microscopy

We further investigate the formed crystalline phases in the 13.3 J/mm^3 rotating vector cuboid, the one with the most intense Bragg reflections in Fig. 3, by SEM analysis. Figure 4a provides a back-scattered electron (BSE) image that features apparent amorphous regions, which can be identified by their homogeneous, contrast-free appearance, and regions of crystalline precipitates with two distinctly

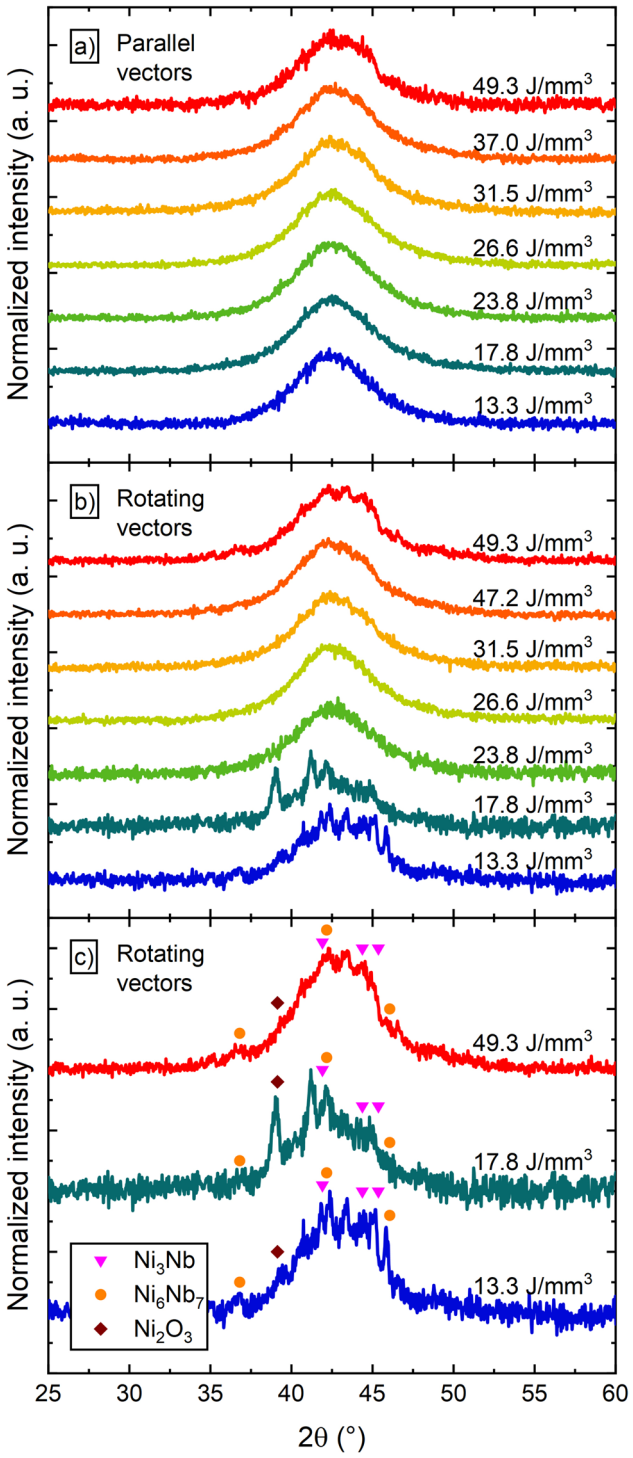

Fig. 3 Screening of the structure via XRD. **a** Parallel vector cuboids show mostly Bragg reflection-free diffractograms with broad, glass-typical halos, only the cuboid with the highest E_V shows slight reflections that indicate crystallinity. **b** Rotating vector samples show slightly more Bragg reflections for low and high E_V values, indicating higher loads of crystallinity. **c** The rotating vector cuboids with the most distinct reflections are shown here in detail to identify the crystalline compounds

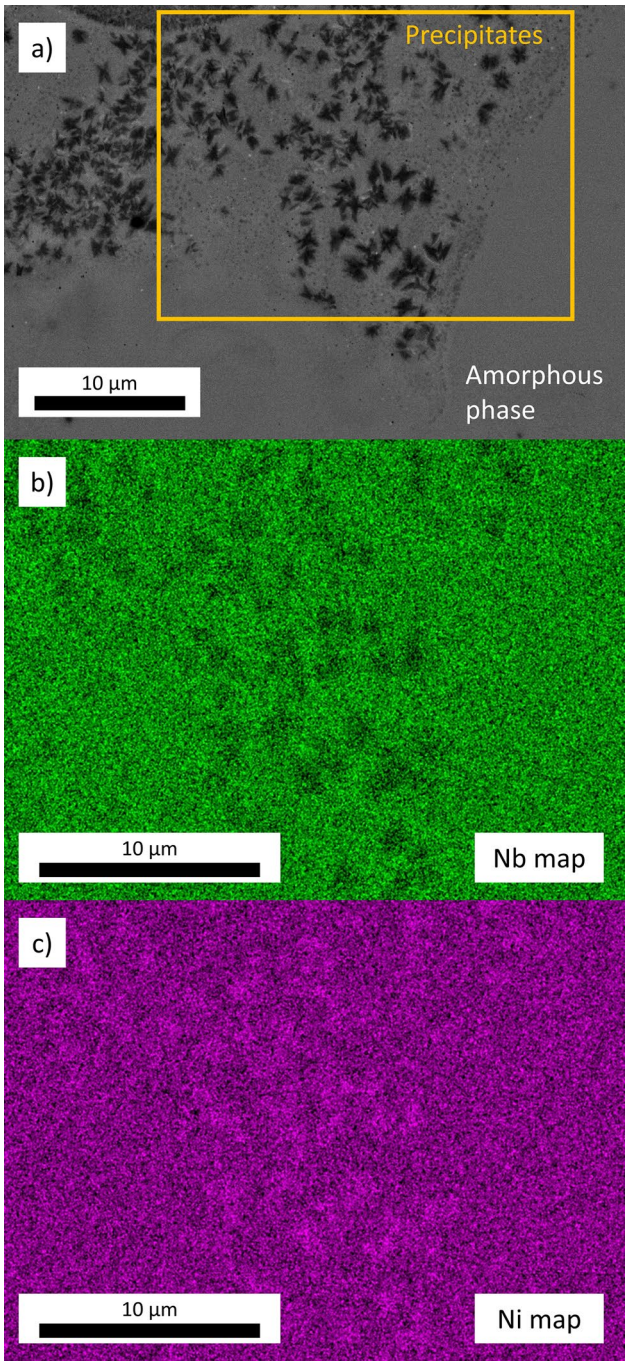

Fig. 4 SEM pictures taken on the 13.3 J/mm^3 rotating vector sample that was shown to feature distinct Bragg reflections in **b** and **c**. **a** A BSE picture of an amorphous region (homogenous) next to a group of nm-scale crystalline precipitates. The elemental maps in **b** and **c** indicate Nb depletion and Ni enrichment in these, which hinds towards the XRD-confirmed Ni_3Nb as composition

different size distributions. More precisely, equiaxed dendritic precipitates of up to 2 µm in size are embedded in a dense field of nano-precipitations that appear as black dots. All crystals are too small for proper chemical analysis by EDX, yet elemental mapping allows at least a qualitative investigation of the larger dendrites. Therefore, the region marked by the yellow frame in Fig. 4a is further EDX scanned, the resulting elemental maps for Ni and Nb are given in Fig. 4b, c. The dendritic precipitates clearly show a depletion of Nb and enrichment in Ni, rendering the XRD-confirmed Ni_3Nb as the most probable composition.

The relatively large precipitation size further indicates that they formed at elevated temperatures, where the fast dynamics of the liquid allowed for pronounced crystal growth [35]. Hence, these larger precipitates likely formed either during the initial cooling of the melt or in the 'inner region' of the heat affected zone, in direct contact with the melt pool. Both possibilities could be promoted by the earlier discussed heat accumulation effects in this 13.3 J/mm^3 sample. Such a formation of Ni_3Nb precipitates at elevated temperatures would be consistent with in-situ HEXRD undercooling experiments on levitated droplets of $Ni_{62}Nb_{38}$, in which Ni_3Nb appears as the primary phase [21]. It would also align with CALPHAD calculations of the Ni–Nb system, which show that the driving force for primary crystallization from liquid $Ni_{62}Nb_{38}$ is much larger for the Ni_3Nb phase than for the Ni_6Nb_7 phase [36]. In contrast, the smaller, nm-sized precipitates, visible in Fig. 4a, rather suggest crystallization at lower temperatures, where crystal growth is kinetically limited. Hence, these nanocrystals most likely form in the 'outer regions' of heat affected zone, with larger distance to the melt pool [10, 12, 37].

3.4 Narrowing down the optimal parameter range by calorimetric screening

Based on the XRD results, parallel vectors appear to be the more promising scanning strategy to achieve fully amorphous $Ni_{62}Nb_{38}$ samples, since it appears to create less heat accumulation than the rotating vectors strategy. Hence, we focus on the parallel vector samples in the following and use DTA temperature scanning to investigate the amount of amorphous phase in the printed samples quantitatively. The results are presented in Fig. 5. The black and grey DTA curves in Fig. 5a are taken from [27] and represent an as-cast reference formed by conventional suction casting as well as the powder feedstock material used for PBF-LB/M with a fraction of 20–63 µm. The crystallization enthalpies, ΔH_x, are determined by integration over the exothermal crystallization event (dotted lines) and are found to be virtually identical with a value of about − 4.60 kJ/g-atom, as it is typical for fully amorphous $Ni_{62}Nb_{38}$ [21]. The DTA curves of the powder and the as-cast material are further compared with the two PBF-LB/M-formed cuboids that show the highest and lowest measured crystallization enthalpies, which are the 17.8 J/mm^3 cuboid and the 49.3 J/mm^3 cuboid. The first one features a ΔH_x of − 4.08 kJ/g-atom, the second one

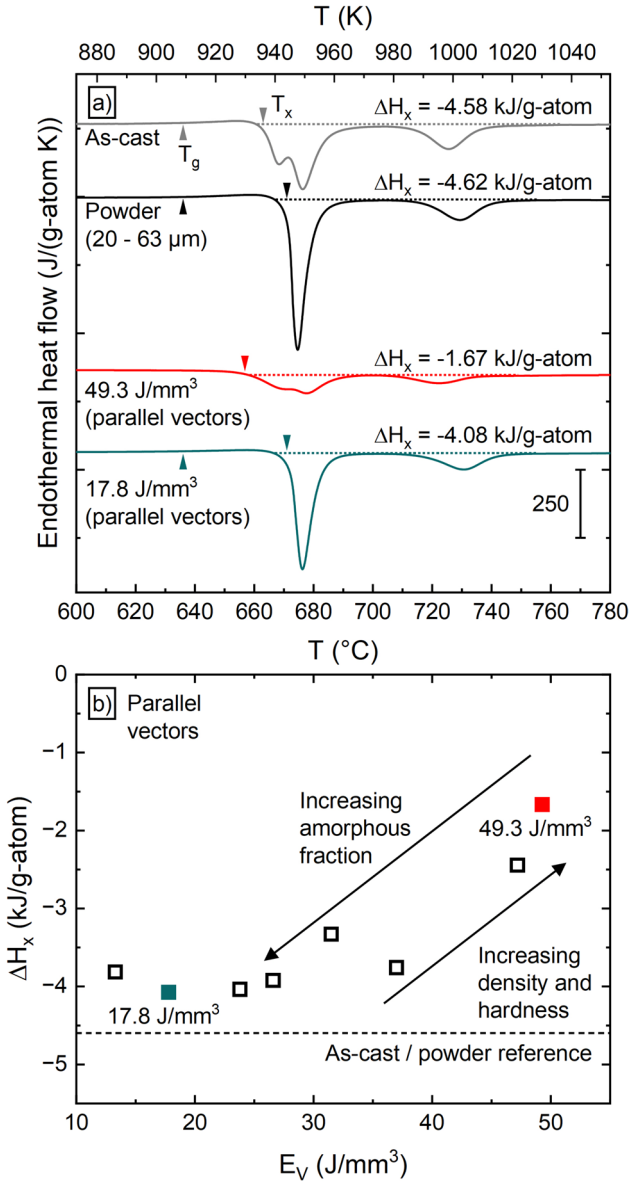

Fig. 5 **a** DTA temperature scans of an as-cast reference and the used powder, taken from [27], in comparison to the scans of the 49.3 and 17.8 J/mm^3 parallel vector cuboids. T_g and T_x are determined by the tangent method (arrows), ΔH_x is determined by integration (dotted lines). **b** All determined ΔH_x values of the parallel vector cuboids as a function of E_V. The cuboids known from **a** are highlighted by color. With values of about 20 J/mm^3, the PBF-LB/M samples reach almost 90% of the reference ΔH_x of −4.60 kJ/g-atom (dashed line), indicating mostly amorphous samples. With rising E_V, relative density and hardness might increase (see Fig. 2), yet, crystallinity also increases

a ΔH_x of only −1.67 kJ/g-atom. This corresponds to 89% and 36% of the reference crystallization enthalpy (4.60 kJ/g-atom), accordingly implying crystalline fractions of 11% and 64%. Considering the mostly peak-free diffractograms in Fig. 3a, the DTA findings demonstrate again that calorimetry can provide better sensitivity and resolution than conventional XRD to detect the presence of (nano-)crystalline fractions in additively formed BMGs [11, 16, 38]. This can be explained by the usually weak scattering signal of nanocrystallites as well as by the fact that calorimetric analysis incorporates the whole sample volume, therefore leading to a more representative, volume-averaged picture than the surface-localized XRD analysis.

While the rather crystal-loaded 49.3 J/mm^3 sample shows no detectable glass transition in the DTA scan, the as-cast, powder, and 17.8 J/mm^3 samples all show a glass transition onset, T_g, of 909 K, as indicated by the arrows in Fig. 5a. Yet, the powder material and the almost fully amorphous 17.8 J/mm^3 parallel vector cuboid are distinctly more thermally stable against crystallization upon heating than the high-purity as-cast reference, since their onset temperature of crystallization, T_x, is 8 K higher (942 K) as in case of the as-cast sample (936 K). Here, the oxygen content plays a decisive role. While the as-cast material shows low levels of oxygen contamination (191 wt-ppm), powder and PBF-LB/M-formed samples feature distinctly higher contamination (863 wt-ppm and above) due to the high oxygen uptake that stems from the large surface-to-volume ratio of the powder particles [27]. Upon heating from the glassy state, the primary crystallization of high-purity Ni–Nb metallic glasses is usually attributed to a metastable crystalline M-phase [36, 39], corresponding to the first separate crystallization event of the as-cast reference in Fig. 5a. As discussed in [27], the increased oxygen content in the powder and AM-formed parts seems to destabilize the primary M-phase, therefore, delaying its formation upon heating, which increases the thermal stability of the supercooled liquid (SCL). Such SCL stabilization effects are well-known from other BMG microalloying approaches with small-size atomic species like Si in CuTi-based systems [40], S in several BMG formers [41, 42], or P in the present Ni–Nb system [21]. The oxygen-driven destabilization of the M-phase renders it possible that Ni_3Nb also becomes the primary phase upon heating, since it was already shown to be the second phase in high-purity $Ni_{62}Nb_{38}$ after the M-phase has formed [39]. Hence, it could be speculated that the nanocrystalline precipitates shown in Fig. 4a next to the large equiaxed Ni_3Nb dendrites consist of the Ni_3Nb phase as well.

Figure 5b summarizes the DTA screening of the parallel vector sample set by plotting ΔH_x as a function of E_V to determine the amount of amorphous phase in the printed samples. The 17.8 J/mm^3 and 49.3 J/mm^3 samples are highlighted in their respective colors from Figs. 3a and 5a. On the one hand, the largest amount of amorphous phase of up to 89% can be found for lower E_V values of roughly 20 J/mm^3. Higher volume energy densities promote increased crystallinity as previously suggested by the XRD results. On the other hand, increased E_V values are needed to achieve full compaction and optimized hardness, as demonstrated in Fig. 2.

3.5 Recapitulatory considerations

We demonstrate that the binary $Ni_{62}Nb_{38}$ BMG former can be processed successfully by PBF/LB-M additive manufacturing, reaching exceptional hardness levels and amorphization degrees of almost 90%. Furthermore, the present parameter study allows us to formulate two main issues that future PBF-LB/M studies must solve to establish PBF-LB/M-formed $Ni_{62}Nb_{38}$ for practical use. First, process parameter optimization has to achieve full amorphization while also ensuring high sample density. While the present results may render both aspects to be antagonistic, it shall be recalled that the low amount of available powder [27] restricts the parameter optimization to first order approaches, here performed in form of a simple variation of E_V. Larger amounts of powder feedstocks will allow advanced processing approaches like two-step scanning [43], which separates material densification and vitrification in two different scanning steps. Second, crack formation can be identified as a major issue for additively formed $Ni_{62}Nb_{38}$. Thereby, the material-typical high modulus and hardness inevitably go hand in hand with increased brittleness, rendering the PBF/LB-M-formed samples prone to crack formation due to process-induced internal stresses [16]. Here, optimization approaches like the already mentioned two-step scanning [43] or changes regarding the used substrate material [9] might help to reduce stress states. Also, the comparably high T_g of Ni–Nb-alloys might induce increased stresses between sample and substrate, necessitating more in-depth testing of different substrate preheating approaches to diminish these stresses, as reported in [16].

4 Conclusions

To sum up, the present parameter study allows to create almost fully amorphous $Ni_{62}Nb_{38}$ samples via PBF-LB/M, which is a quite promising result considering the system's relatively low critical casting thickness of 2 mm. Nevertheless, porosity and crack formation are challenges that need to be solved and balanced through advanced processing approaches tested in follow-up studies. After resolving these issues, amorphous $Ni_{62}Nb_{38}$ will constitute an extremely potent choice for the additive manufacturing of highly robust products, due to the system's outstanding strength and hardness.

Acknowledgements We would like to thank Martina Stemmler for her assistance regarding SEM and XRD analysis. Instrumentation and technical assistance for this work were provided by the Service Center X-ray Diffraction, with financial support from Saarland University and German Science Foundation (project number INST 256/349-1).

Funding Open Access funding enabled and organized by Projekt DEAL.

Data availability All data needed to evaluate the conclusions in the paper are present in the paper. Additional data related to this work may be requested from the authors.

Declarations

Conflict of interest On behalf of all authors, the corresponding author states that there is no conflict of interest.

References

1. Telford M (2004) The case for bulk metallic glass. Mater Today 7:36–43. https://doi.org/10.1016/S1369-7021(04)00124-5
2. Scipioni Bertoli U, Guss G, Wu S et al (2017) In-situ characterization of laser-powder interaction and cooling rates through high-speed imaging of powder bed fusion additive manufacturing. Mater Des 135:385–396. https://doi.org/10.1016/j.matdes.2017.09.044
3. Hooper PA (2018) Melt pool temperature and cooling rates in laser powder bed fusion. Addit Manuf 22:548–559. https://doi.org/10.1016/j.addma.2018.05.032
4. Pauly S, Löber L, Petters R et al (2013) Processing metallic glasses by selective laser melting. Mater Today 16:37–41. https://doi.org/10.1016/j.mattod.2013.01.018
5. Li XP, Roberts MP, O'Keeffe S, Sercombe TB (2016) Selective laser melting of Zr-based bulk metallic glasses: processing, microstructure and mechanical properties. Mater Des 112:217–226. https://doi.org/10.1016/j.matdes.2016.09.071
6. Wegner J, Frey M, Stiglmair P et al (2019) Mechanical properties of honeycomb structured zr-based bulk metallic glass specimens fabricated by laser powder bed fusion. South Afr J Ind Eng 30(3):32–40. https://doi.org/10.7166/30-3-2265
7. Wegner J, Frey M, Busch R, Kleszczynski S (2021) Additive manufacturing of a compliant mechanism using Zr-based bulk metallic glass. Addit Manuf Lett 1:100019. https://doi.org/10.1016/j.addlet.2021.100019
8. Thorsson L, Unosson M, Teresa Pérez-Prado M et al (2022) Selective laser melting of a Fe-Si-Cr-B-C-based complex-shaped amorphous soft-magnetic electric motor rotor with record dimensions. Mater Des 215:110483. https://doi.org/10.1016/j.matdes.2022.110483
9. Wegner J, Kleszczynski S, Frey M, et al (2018) Parameterstudie zur Verarbeitung metallischer Gläser auf Zr-Basis mit dem Laser-Strahlschmelzverfahren. In: Proceedings of the 15th Rapid. Tech Conference
10. Marattukalam JJ, Pacheco V, Karlsson D et al (2020) Development of process parameters for selective laser melting of a Zr-based

bulk metallic glass. Addit Manuf 13:101124. https://doi.org/10.1016/j.addma.2020.101124
11. Wegner J, Frey M, Piechotta M et al (2021) Influence of powder characteristics on the structural and the mechanical properties of additively manufactured Zr-based bulk metallic glass. Mater Des 209:109976. https://doi.org/10.1016/j.matdes.2021.109976
12. Pacheco V, Karlsson D, Marattukalam JJ et al (2020) Thermal stability and crystallization of a Zr-based metallic glass produced by suction casting and selective laser melting. J Alloys Compd 825:8. https://doi.org/10.1016/j.jallcom.2020.153995
13. Sohrabi N, Jhabvala J, Kurtuldu G, et al (2021) Characterization, mechanical properties and dimensional accuracy of a Zr-based bulk metallic glass manufactured via laser powder-bed fusion. 199:8. https://doi.org/10.1016/j.matdes.2020.109400
14. Li B, Yakubov V, Nomoto K et al (2024) Superior mechanical properties of a Zr-based bulk metallic glass via laser powder bed fusion process control. Acta Mater 266:119685. https://doi.org/10.1016/j.actamat.2024.119685
15. Wang P, Pauly S, Deng L et al (2017) Selective laser melting of a Ti-based bulk metallic glass. Mater Lett 212:346–349. https://doi.org/10.1016/j.matlet.2017.10.130
16. Frey M, Wegner J, Barreto ES et al (2023) Laser powder bed fusion of Cu-Ti-Zr-Ni bulk metallic glasses in the Vit101 alloy system. Addit Manuf 66:8. https://doi.org/10.1016/j.addma.2023.103467
17. Heinrich J, Busch R, Nonnenmacher B (2012) Processing of a bulk metallic glass forming alloy based on industrial grade Zr. Intermetallics 25:1–4. https://doi.org/10.1016/j.intermet.2012.02.011
18. Frey M, Wegner J, Neuber N et al (2021) Thermoplastic forming of additively manufactured Zr-based bulk metallic glass: a processing route for surface finishing of complex structures. Mater Des 198:1–8. https://doi.org/10.1016/j.matdes.2020.109368
19. Ruhl RC, Giessen BC, Cohen M, Grant NJ (1967) New microcrystalline phases in the NbNi and TaNi systems. Acta Metall 15:1693–1702. https://doi.org/10.1016/0001-6160(67)90060-0
20. Xia L, Li WH, Fang SS et al (2006) Binary Ni-Nb bulk metallic glasses. J Appl Phys 99:58–61. https://doi.org/10.1063/1.2158130
21. Ruschel LM, Gross O, Bochtler B et al (2023) Ni-Nb-P-based bulk glass-forming alloys: superior material properties combined in one alloy family. Acta Mater 6:118968. https://doi.org/10.1016/j.actamat.2023.118968
22. Choi-Yim H, Xu D, Johnson WL (2003) Ni-based bulk metallic glass formation in the Ni-Nb-Sn and Ni-Nb-Sn-X (X = B, Fe, Cu) alloy systems. Appl Phys Lett 82:1030–1032. https://doi.org/10.1063/1.1544434
23. Hu HT, Chen LY, Wang XD et al (2008) Formation of Ni-Nb-Zr-X (X = Ti, Ta, Fe, Cu, Co) bulk metallic glasses. J Alloys Compd 460:714–718. https://doi.org/10.1016/j.jallcom.2008.01.075
24. Tian J, Jiang Z (2021) Exploring new strategies for ultrahigh strength steel via tailoring the precipitates. Front Mater 8:1–7. https://doi.org/10.3389/fmats.2021.797798
25. Jones MR, DelRio FW, Pegues JW et al (2021) Additive manufacturing of high-strength multiphase nanostructures in the binary Ni–Nb system for the discovery of new types of superalloys. J Mater Res 36:3167–3181. https://doi.org/10.1557/s43578-021-00290-7
26. Sohrabi N, Jhabvala J, Logé RE (2021) Additive manufacturing of bulk metallic glasses—process, challenges and properties: a review. Metals (Basel) 11:8
27. Barreto ES, Frey M, Matthias L et al (2024) Gas atomization of fully-amorphous Ni62Nb38 powder. Mater Lett 357:135798. https://doi.org/10.1016/j.matlet.2023.135798
28. Mukherjee T, DebRoy T (2018) Mitigation of lack of fusion defects in powder bed fusion additive manufacturing. J Manuf Process 36:442–449. https://doi.org/10.1016/j.jmapro.2018.10.028
29. Oliveira JP, LaLonde AD, Ma J (2020) Processing parameters in laser powder bed fusion metal additive manufacturing. Mater Des 193:1–12. https://doi.org/10.1016/j.matdes.2020.108762
30. Shrestha S, Chou K (2022) Formation of keyhole and lack of fusion pores during the laser powder bed fusion process. Manuf Lett 32:19–23. https://doi.org/10.1016/j.mfglet.2022.01.005
31. Mojumder S, Gan Z, Li Y et al (2023) Linking process parameters with lack-of-fusion porosity for laser powder bed fusion metal additive manufacturing. Addit Manuf 68:103500. https://doi.org/10.1016/j.addma.2023.103500
32. Mercelis P, Kruth JP (2006) Residual stresses in selective laser sintering and selective laser melting. Rapid Prototyp J 12:254–265. https://doi.org/10.1108/13552540610707013
33. Shiomi M, Osakada K, Nakamura K et al (2004) Residual stress within metallic model made by selective laser melting process. CIRP Ann - Manuf Technol 53:195–198. https://doi.org/10.1016/S0007-8506(07)60677-5
34. Okamoto H (2008) Nb-Ni (Niobium–Nickel). J Phase Equilibria Diffus 29:210–210. https://doi.org/10.1007/s11669-008-9277-0
35. Schroers J, Busch R, Masuhr A, Johnson WL (1999) Continuous refinement of the microstructure during crystallization of supercooled Zr41Ti14Cu12Ni10Be23 melts. Appl Phys Lett 74:2806–2808. https://doi.org/10.1063/1.124020
36. Stanojevic S, Gallino I, Aboulfadl H et al (2016) Oxidation of glassy Ni-Nb-Sn alloys and its influence on the thermodynamics and kinetics of crystallization. Acta Mater 102:176–186. https://doi.org/10.1016/j.actamat.2015.09.009
37. Yang Z, Markl M, Körner C (2022) Predictive simulation of bulk metallic glass crystallization during laser powder bed fusion. Addit Manuf 59:8. https://doi.org/10.1016/j.addma.2022.103121
38. Wegner J, Frey M, Kleszczynski S, et al (2020) Influence of process gas during powder bed fusion with laser beam of Zr-based bulk metallic glasses. In: 11th CIRP Conference on Photonic Technologies [LANE 2020]. Elsevier B.V., pp 205–210
39. Collins LE, Grant NJ, Vander Sande JB (1983) Crystallization of amorphous Ni60Nb40. J Mater Sci 18:804–814. https://doi.org/10.1007/BF00745579
40. Choi-Yim H, Busch R, Johnson WL (1998) The effect of silicon on the glass forming ability of the Cu47Ti34Zr11Ni8 bulk metallic glass forming alloy during processing of composites. J Appl Phys 83:7993–7997. https://doi.org/10.1063/1.367981
41. Jiang HR, Hu JY, Neuber N et al (2021) Effect of sulfur on the glass-forming ability, phase transformation, and thermal stability of Cu-Zr-Al bulk metallic glass. Acta Mater 212:116923. https://doi.org/10.1016/j.actamat.2021.116923
42. Kuball A, Gross O, Bochtler B, Busch R (2018) Sulfur-bearing metallic glasses: a new family of bulk glass-forming alloys. Scr Mater 146:73–76. https://doi.org/10.1016/j.scriptamat.2017.11.011
43. Żrodowski Ł, Wróblewski R, Leonowicz M et al (2023) How to control the crystallization of metallic glasses during laser powder bed fusion? Towards part-specific 3D printing of in situ composites. Addit Manuf 76:8. https://doi.org/10.1016/j.addma.2023.103775